

# Pourbaix Machine Learning Framework Identifies Acidic Water Oxidation Catalysts Exhibiting Suppressed Ruthenium Dissolution

Jehad Abed,<sup>○</sup> Javier Heras-Domingo,<sup>○</sup> Rohan Yuri Sanspeur,<sup>○</sup> Mingchuan Luo, Wajdi Alnoush, Debora Motta Meira, Hsiaotsu Wang, Jian Wang, Jigang Zhou, Daojin Zhou, Khalid Fatih, John R. Kitchin, Drew Higgins, Zachary W. Ulissi,\* and Edward H. Sargent\*



Cite This: *J. Am. Chem. Soc.* 2024, 146, 15740–15750



Read Online

ACCESS |



Metrics & More

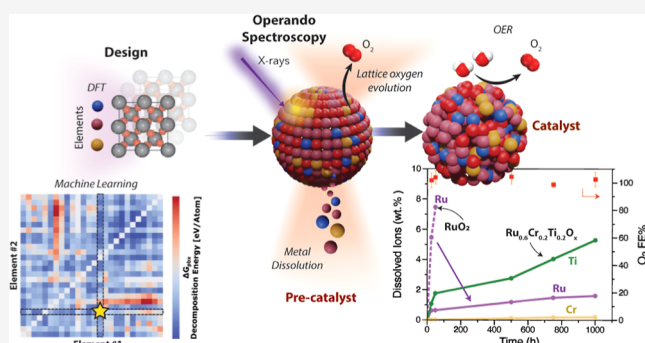


Article Recommendations



Supporting Information

**ABSTRACT:** The demand for green hydrogen has raised concerns over the availability of iridium used in oxygen evolution reaction catalysts. We identify catalysts with the aid of a machine learning-aided computational pipeline trained on more than 36,000 mixed metal oxides. The pipeline accurately predicts Pourbaix decomposition energy ( $G_{\text{pbx}}$ ) from unrelaxed structures with a mean absolute error of 77 meV per atom, enabling us to screen 2070 new metallic oxides with respect to their prospective stability under acidic conditions. The search identifies  $\text{Ru}_{0.6}\text{Cr}_{0.2}\text{Ti}_{0.2}\text{O}_2$  as a candidate having the promise of increased durability: experimentally, we find that it provides an overpotential of 267 mV at 100  $\text{mA cm}^{-2}$  and that it operates at this current density for over 200 h and exhibits a rate of overpotential increase of 25  $\mu\text{V h}^{-1}$ . Surface density functional theory calculations reveal that Ti increases metal–oxygen covalency, a potential route to increased stability, while Cr lowers the energy barrier of the  $\text{HOO}^*$  formation rate-determining step, increasing activity compared to  $\text{RuO}_2$  and reducing overpotential by 40 mV at 100  $\text{mA cm}^{-2}$  while maintaining stability. In situ X-ray absorption spectroscopy and ex situ ptychography-scanning transmission X-ray microscopy show the evolution of a metastable structure during the reaction, slowing Ru mass dissolution by 20 $\times$  and suppressing lattice oxygen participation by >60% compared to  $\text{RuO}_2$ .



## INTRODUCTION

Proton exchange membrane (PEM) electrolyzers, which offer higher current densities (1–3  $\text{A cm}^{-2}$ ), greater hydrogen pressure (>30 bar), and a significantly smaller footprint (40 $\times$  smaller), are anticipated to play a significant role in the growth of commercial green hydrogen production, presenting an alternative to conventional alkaline water electrolyzers. However, the cost of the membrane electrode-assembly, which constitutes around 30% of the total stack cost of PEM, is driven up by the use of precious group metal catalysts. Iridium oxide ( $\text{IrO}_2$ ) is currently the only oxygen evolution reaction (OER) electrocatalyst that can withstand harsh acidic conditions at the anode, but its high cost and increasing demand pose a challenge. Therefore, the design of efficient and stable Ir-free OER electrocatalysts is crucial for the future of large-scale hydrogen production.

Ru-based OER catalysts offer a promising alternative to Ir because: (i) Ru is  $\sim 100\times$  more abundant and today costs  $\sim 8\times$  less,<sup>1</sup> (ii) Ru has higher intrinsic activity than Ir,<sup>1</sup> and (iii) earth-abundant acid OER catalysts today, unlike Ru, are catalytically poor (600–700 mV overpotential at currents <100  $\text{mA cm}^{-2}$ ) or only quasi-stable even at high mass loadings.<sup>2</sup> However, the overoxidation of Ru atoms during the OER

results in the formation of soluble  $\text{Ru}^{>4+}$  species, which can significantly shorten the lifetime of the catalyst. Most reports in the literature have relied on chemical intuition to improve the design of OER electrocatalysts using strategies such as alloying and doping with  $\text{Ir}^3$  or 3d metals<sup>4,5</sup> and engineering lattice strain<sup>6</sup> to redistribute the surface charge and reduce over-oxidation of Ru. Although these strategies have proven to result in an improved activity (i.e., overpotential for the OER at 10  $\text{mA cm}^{-2}$ ), the stability was limited to a few hours at >10  $\text{mA cm}^{-2}$ .

In light of the superior OER activity of  $\text{RuO}_2$  and the persistent challenges associated with Ru dissolution and electrochemical stability, our goal is to screen the vast chemical space of multimetal oxides to enhance  $\text{RuO}_2$  catalyst through alloying. Implementing neural nets to accelerate expensive density functional theory (DFT) have shown promise guiding

Received: January 28, 2024

Revised: May 22, 2024

Accepted: May 23, 2024

Published: June 3, 2024



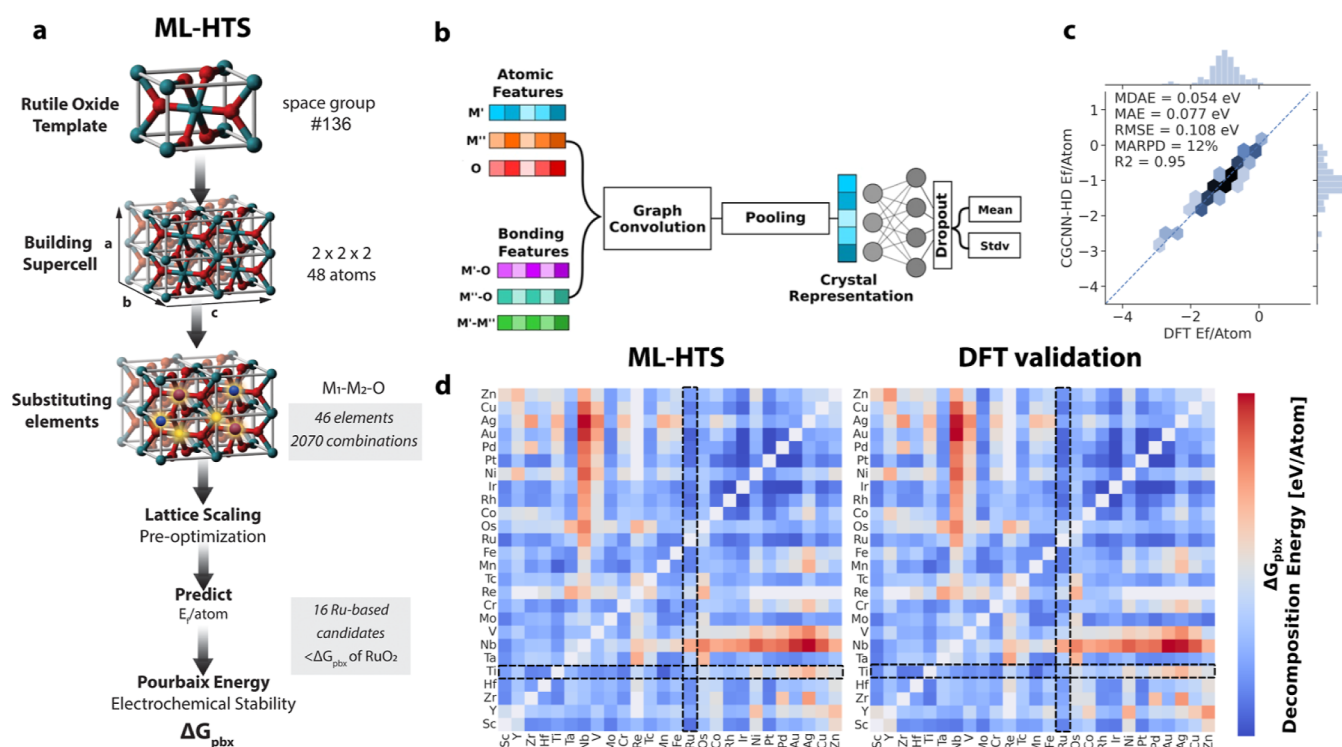


**Figure 1.** (a) Diagram illustrating the workflow of the machine learning high-throughput screening (ML-HTS) pipeline, employed to predict the Pourbaix electrochemical stability ( $\Delta G_{\text{pbx}}$ ) for 2070 rutile oxide structures. Sixteen candidate materials are narrowed down by choosing Ru-based rutile oxides with a lower  $\Delta G_{\text{pbx}}$  than  $\text{RuO}_2$ . (b) CGCNN-HD model architecture. A validation of the ML-HTS predictions is performed using DFT on a 34% subset of the structures, which includes 26 elements and 676 oxides. (c) Parity plot showing the performance of the CGCNN-HD model as a surrogate model for electrochemical stability against DFT formation energy per atom ( $E_f/\text{atom}$ ). (d) CGCNN-HD heatmaps of  $\Delta G_{\text{pbx}}$  (Left) vs DFT validation stability heatmap (right) for the subset. Highlighted in the dashed area is Ru–Ti as the most stabilizing with a nonprecious metal. \* In the heatmaps, stable is indicated in blue and unstable is red.

the discovery of novel materials.<sup>7–9</sup> However, the challenge lies in predicting accurately the Pourbaix stability of oxides while mitigating the risk of false positive predictions and the low reliability of predictions starting from unrelaxed DFT structures. In this work, we train a CGCNN-HD on more than 36,000 mixed metal oxides, which were uniformly preprocessed and scaled using a lattice scaling approach, ensuring rapid and cost-effective optimization of the lattice for both training and new hypothetical materials. Although high-throughput density functional theory offers precise simulations, its computational cost escalates rapidly to prohibitive levels for extensive data sets, whereas machine learning (ML) models present a cost-effective alternative, enabling rapid, computationally efficient, assessments without significant loss of accuracy. Then, we use the model to predict the Pourbaix electrochemical stability of 2070 hypothetical and unrelaxed oxide structures. Afterward, we focused our search on Ru-based oxides and used metal–oxygen covalency, calculated by DFT, as a second descriptor for bulk stability. We show that by substituting transition-metal atoms in the  $\text{RuO}_2$  lattice while preserving the lattice, we could modulate the Ru–M–O covalency rendering a more rigid oxide framework and larger thermodynamic/kinetics barriers for metal dissolution. We computationally identified  $\text{Ru}_{0.6}\text{Cr}_{0.2}\text{Ti}_{0.2}\text{O}_x$  as the best candidate and experimentally synthesized the materials for testing. Upon the OER evaluation, we discover that doping with Ti stabilizes  $\text{RuO}_2$  and increases the metal–oxygen covalency of the structure. We investigate the structural change of the candidate during the reaction by in situ X-ray absorption

spectroscopy (XAS) and ex situ scanning transmission X-ray microscopy (STXM) spectroptychography. Additionally, we use inductively coupled plasma-atomic emission spectroscopy (ICP-AES) and in situ differential electrochemical mass spectroscopy (DEMS) to quantify ruthenium dissolution and lattice oxygen participation, linking these factors to understanding performance degradation. Finally, we use DFT to study the role of Ti and Cr on the stability and activity and explain the synergistic effect of these metals on the performance of  $\text{RuO}_2$ .

## RESULTS AND DISCUSSION

**Pourbaix Surrogate Model Training.** Our primary objective is to develop a ML model capable of accurately approximating the Pourbaix electrochemical stability of hypothetical, unseen structures. To achieve this, we trained a CGCNN-HD<sup>10</sup> surrogate model (Figures 1b, S1 and Table S1) to predict the energy of formation per atom ( $E_f/\text{atom}$ ), serving as a proxy for electrochemical stability; we refer to this energy as the Pourbaix energy in this work ( $\Delta G_{\text{pbx}}$ ). We utilized a data set of 36,465 metal oxide bulk structures from the Materials Project<sup>11</sup> for training, validation, and testing. To maintain a consistent level of DFT theory for training, all calculations for Pourbaix stability of reference phases were exclusively conducted from the Materials Project data set. Additionally, we chose the CGCNN-HD model due to its high effectiveness when trained on domain-specific targets like  $E_f/\text{atom}$ , which yields accurate predictions suitable for the scope and size of the training data in this work. All structures

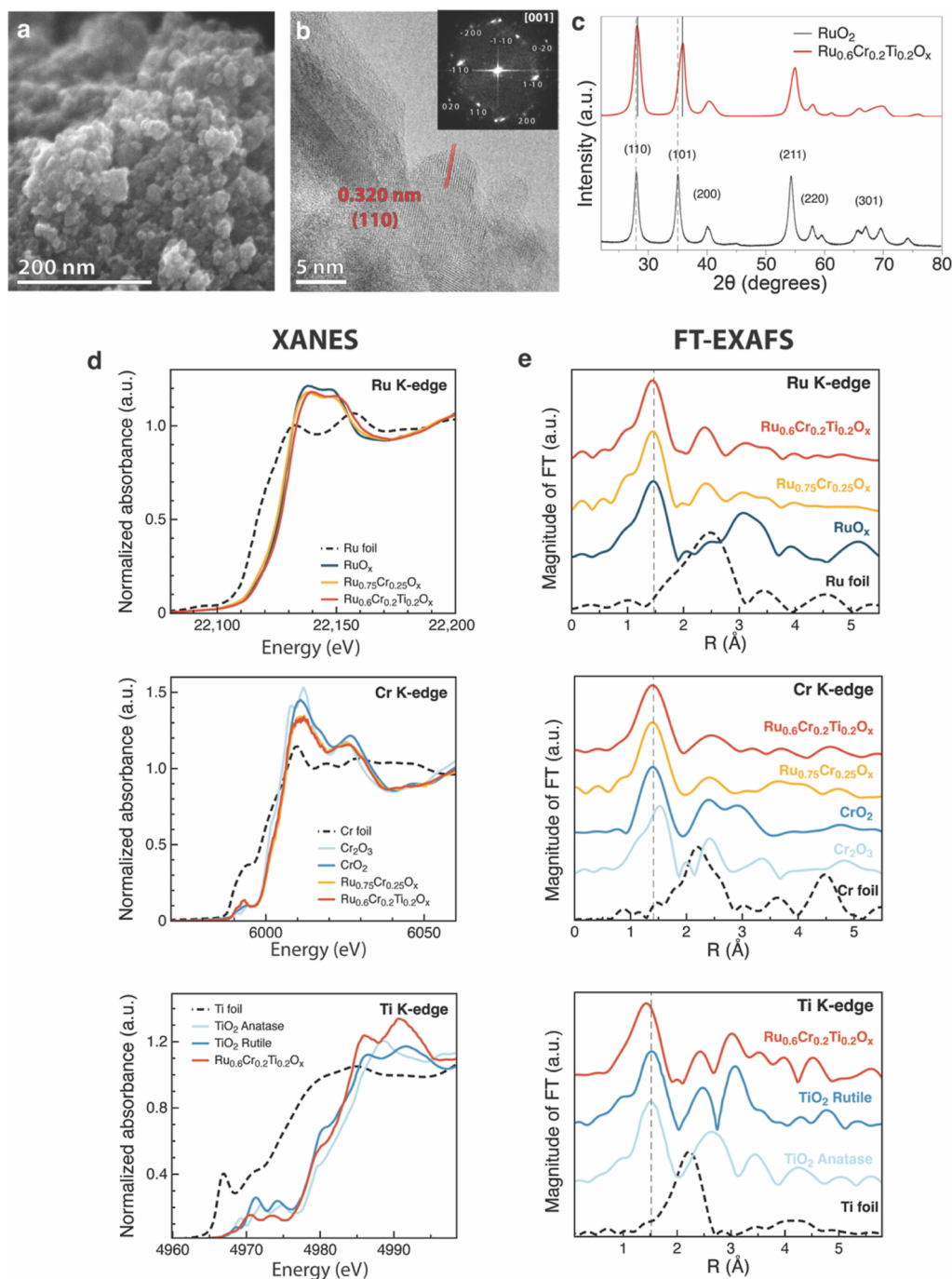


**Figure 2.** (a) High-resolution SEM image of an agglomerate of nanoparticles for  $\text{Ru}_{0.6}\text{Cr}_{0.2}\text{Ti}_{0.2}\text{O}_x$ . (b) High-resolution TEM image of small  $\text{Ru}_{0.6}\text{Cr}_{0.2}\text{Ti}_{0.2}\text{O}_x$  nanoparticles. Inset is the FFT electron diffraction pattern of the selected region with a [001] zone axis. (c) XRD patterns of  $\text{Ru}_{0.6}\text{Cr}_{0.2}\text{Ti}_{0.2}\text{O}_x$  and rutile  $\text{RuO}_2$ . (d) X-ray absorption near-edge structure (XANES) of  $\text{Ru}_{0.6}\text{Cr}_{0.2}\text{Ti}_{0.2}\text{O}_x$  (red),  $\text{Ru}_{0.6}\text{Cr}_{0.4}\text{O}_x$  (yellow), and  $\text{RuO}_x$  (dark blue). (e) Phase-uncorrected Fourier transform-extended X-ray absorption fine structure (FT-EXAFS) of  $\text{Ru}_{0.6}\text{Cr}_{0.2}\text{Ti}_{0.2}\text{O}_x$  (red),  $\text{Ru}_{0.6}\text{Cr}_{0.4}\text{O}_x$  (yellow), and  $\text{RuO}_x$  (dark blue).

underwent a preprocessing and scaling procedure using the lattice scaling approach proposed by Chu et al.,<sup>18</sup> which is based on prior chemical bond statistics. This method allowed us to swiftly preoptimize the lattice for all structures (Figure 1a), bypassing the need for costly DFT optimization and ensuring consistency in both training and hypothetical material generation. The trained model was employed to predict both the mean ( $\mu$ ) and standard deviation ( $s$ ) for each material. To minimize the error caused by nonideal structures, we shifted the predicted property within a 95% confidence interval ( $\mu -$

2s) instead of using the mean of dropout sampling directly. Although this approach might result in mislabeling a few false positives, it significantly increased the overall screening throughput. This trade-off is acceptable because the additional cost of having false positives is relatively low compared to the brute-force DFT approach.<sup>10,12</sup> Details on the model's architecture and hyperparameter tuning strategy are further described in the notes in the Supporting Information (see Supporting Information, Section S1).



### Screening Candidates with the Surrogate Model.

With the trained model in place, we embarked on an exploration of the  $M-M_2-O$  chemical space, maintaining the rutile oxide structure constant while seeking metal oxide compositions with enhanced electrochemical stability  $\Delta G_{\text{pbx}}$  compared to  $\text{RuO}_2$ . More specifically, we substituted 46 elements in the oxide structure to generate a data set of 2070 hypothetical compounds using the 136 space group (Figures 1a and S3). The surrogate model demonstrated a promising prediction Pourbaix energy accuracy MAE 0.077  $E_f/\text{atom}$  starting from unrelaxed structures (see Supporting Information, Section S2), enabling us to rapidly determine the electrochemical stability of a vast chemical space. We compare the accuracy of predicting Pourbaix energy using the CGCNN-HD model with respect to DFT on a large subset of hypothetical structures (26 elements, 676 binary oxides, and 34% of the total data set), as shown in the parity plot (Figure 1c) and heatmaps (Figure 1d), which showed a significant correlation between both methods. From the total data set of 2070 compounds, 195 rutile oxide structures were selected based on energy above hull ( $E_{\text{hull}}$ ) criteria, filtering out structures exceeding 0.5 eV (see Supporting Information, Tables S2 and S3).

We then calculated the metal–oxygen covalency of all compositions containing Ru using the crystal orbital Hamilton population (COHP) analysis<sup>13,14</sup> (see Supporting Information, Table S3). Computational screening revealed that doping Ti in  $\text{RuO}_2$  significantly reduced  $\Delta G_{\text{pbx}}$  compared to  $\text{RuO}_2$  and resulted in the most substantial increase in metal–oxygen covalency (+10.7%). This was followed by Sn (+9.05%) and Ge (+8.6%). Interestingly, Wang et al. identified computationally 68 oxide structures, from the Material Project data set, containing either Ti, Sn, or Ge that improved corrosion resistance under acidic water oxidation.<sup>15,16</sup> This further corroborates our results, underscoring Ti, Sn, and Ge as elements of interest for stability improvements.

Cr also appeared in our candidate list of elements improving the Pourbaix stability of  $\text{Ru}-M-\text{O}_2$  (see Supporting Information, Table S3). Additionally, in our previous study, we observed that doping even small amounts of Cr in  $\text{RuO}_2$  improved the specific activity of  $\text{RuO}_2$  without disturbing the rutile lattice.<sup>17</sup> This activity improvement, due to Cr doping, was also noted by Lin et al., but its influence on stability was not clearly explained.<sup>5</sup>

Building on these findings, we chose to concentrate our experimental validation on the  $\text{Ru}-\text{Cr}-\text{Ti}-\text{O}_x$  family of catalysts: computationally, Ti demonstrated the largest computational improvement in both Pourbaix stability and metal–oxygen covalency; and Cr was found to have a dual effect of increasing Pourbaix stability and enhancing activity.

**Synthesis and Performance Optimization.** Using a sol–gel synthesis method, we synthesized the predicted compounds  $\text{Ru}-\text{Cr}-\text{Ti}-\text{O}_x$  and optimized the doping amounts of Cr and Ti in  $\text{Ru}-M_1-M_2-\text{O}_2$  to lower the overpotential and increase the stability. First, we start by tuning the amount of Cr in the catalyst by preparing three samples with 25 atom %, 50 atom %, and 75 atom % of Cr in  $\text{Ru}-M-\text{O}_2$  and experimentally measured the polarization curves (Figure S4). We found that  $\text{Ru}_{0.75}\text{Cr}_{0.25}\text{O}_x$  had the largest decrease in overpotential, approximately 70 mV less than the overpotential of  $\text{RuO}_x$  (at 10  $\text{mA cm}^{-2}$ ) while still preserving the rutile oxide structure as evidenced by XRD (Figure S5). However, as we increased the Cr content in  $\text{RuO}_2$ , we

observed the emergence of an additional oxide phase,  $\text{Cr}_2\text{O}_3$ . This led to a substantial increase in the overpotential because  $\text{Cr}_2\text{O}_3$  is catalytically less active than  $\text{RuO}_2$ . Therefore, we chose doping  $\text{RuO}_2$  with 25 atom % Cr to yield the most substantial enhancement in activity.

Second, we doped Ti in  $\text{Ru}-\text{Cr}-M_2-\text{O}_x$ . Most titanium salts were found to be insoluble and reactive in the solvents used for sol–gel synthesis. However, titanium diisopropoxide bis(acetylacetonate) precursor partially dissolved in ethanol when used in small amounts without reacting in the solution. As a result, we were able to incorporate at most 20% at. Ti in the structure. Larger amounts of the precursor led to disturbing the gelled network of metal cations during the gelation process. High-resolution transmission electron microscopy images confirmed the synthesis of nanoparticle agglomerates with a crystallite size <5 nm and a localized rutile structure as shown by the Fast Fourier transform (FFT) of the crystalline region of the HRTEM image (Figure 2a,b). The XRD pattern showed that  $\text{Ru}_{0.6}\text{Cr}_{0.2}\text{Ti}_{0.2}\text{O}_x$  possessed a rutile structure similar to a commercial  $\text{RuO}_2$  standard (fuel cell store) with wider diffraction peaks suggesting lower crystallinity or smaller average crystallite sizes (Figure 2c). By evaluating the full width at half-maximum of the XRD peaks, the crystallite size of  $\text{Ru}_{0.75}\text{Cr}_{0.25}\text{O}_x$  and  $\text{Ru}_{0.6}\text{Cr}_{0.2}\text{Ti}_{0.2}\text{O}_x$  samples had a smaller value of 3.5–5.0 nm, consistent with HRTEM analysis, compared to 6.1–7.8 nm for commercial  $\text{RuO}_x$  (Table S4). Elemental maps collected by energy-dispersive spectroscopy (EDS) showed a uniform distribution of elements across the particles, suggesting the formation of a mixed metal rutile oxide (Figure S6).

XANES measurements at the Ru K-edge of  $\text{Ru}_{0.75}\text{Cr}_{0.25}\text{O}_x$  and  $\text{Ru}_{0.6}\text{Cr}_{0.2}\text{Ti}_{0.2}\text{O}_x$  did not show any significant shifts in the absorption edge compared to  $\text{RuO}_x$ , implying that the oxidation state of Ru remained close to 4+ after doping with Cr and Ti (Figures 2d and S7). The reduction in the white line intensity of the XANES spectrum suggests that the Ru atoms in the  $\text{RuO}_x$  lattice were replaced with Cr and Ti. The incorporation of Cr and Ti into the surfaces of the samples can also be noticed in the cyclic voltammetry scans of the samples (Figure S10). A clear suppression of the redox peaks indicates a change in the structure of the surface. Furthermore, the edge position and shape of the XANES of Cr and Ti K-edges were comparable to control samples  $\text{CrO}_2$  and  $\text{TiO}_2$ , which corroborates the formation of a rutile structure with an oxidation state close to 4+ for all elements (Figures 2d, S8, and S9).

FT-EXAFS for the synthesized samples and reference samples are shown in Figure 2e as a function of the phase-uncorrected interatomic distance  $R$ . The peak positions of Ru–O at 1.47 Å and Cr–O at 1.42 Å in  $\text{Ru}_{0.75}\text{Cr}_{0.25}\text{O}_x$  and  $\text{Ru}_{0.6}\text{Cr}_{0.2}\text{Ti}_{0.2}\text{O}_x$  samples match well with those of  $\text{RuO}_2$  and  $\text{CrO}_2$  rutile oxide reference samples, reinforcing that the rutile oxide lattice is preserved. Furthermore, we observe a significant negative shift in the Ti–O bond at 1.45 Å for  $\text{Ru}_{0.6}\text{Cr}_{0.2}\text{Ti}_{0.2}\text{O}_x$  compared to 1.52 Å in reference rutile  $\text{TiO}_2$ , suggesting structural distortion in the Ti–O bond due to lattice doping.<sup>18</sup> These observations were further confirmed by fitting the EXAFS signal of  $\text{Ru}_{0.6}\text{Cr}_{0.2}\text{Ti}_{0.2}\text{O}_x$  to a DFT-relaxed crystal structure for  $\text{Ru}-\text{Cr}-\text{Ti}-\text{O}_2$  (Figure 5a). This is the same crystal structure model we used for DFT calculations later in this article to determine the theoretical reactivity. The details of the fitting parameters and model can be found in Figures S11–S13 and Tables S5–S7.

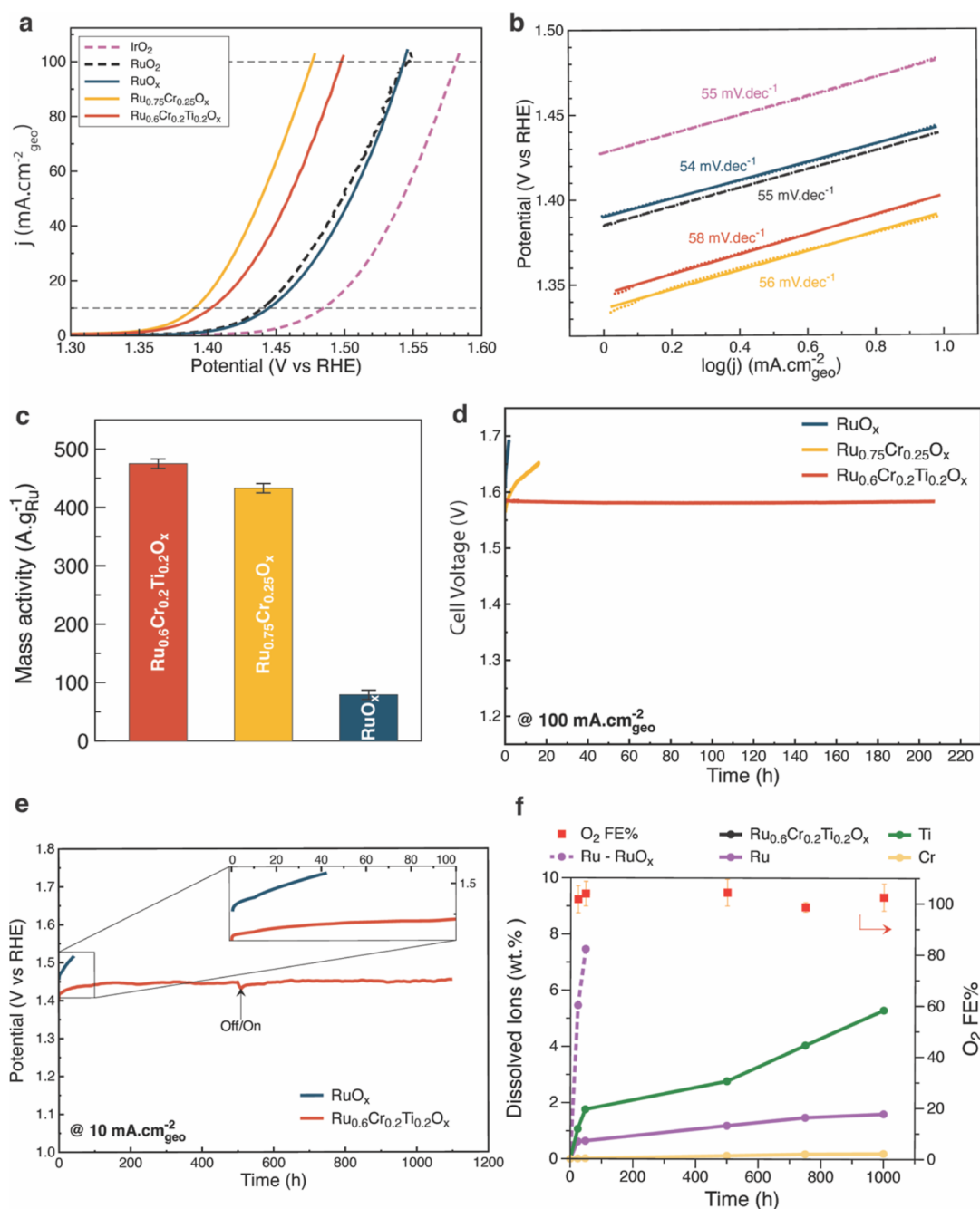


**Figure 3.** (a) Polarization curves for Ru<sub>0.6</sub>Cr<sub>0.2</sub>Ti<sub>0.2</sub>O<sub>x</sub> (red), Ru<sub>0.6</sub>Cr<sub>0.4</sub>O<sub>x</sub> (yellow), and RuO<sub>x</sub> (dark blue) compared to commercial RuO<sub>2</sub> (black, dashed line) and IrO<sub>2</sub> (purple, dashed line) nanoparticles. X-axis is the half-cell potential vs RHE and the y-axis is the current density normalized by geometric area of the electrode. (b) Calculated Tafel slopes in the current density region between 1 and 10 mA·cm<sup>-2</sup><sub>geo</sub> for Ru<sub>0.6</sub>Cr<sub>0.2</sub>Ti<sub>0.2</sub>O<sub>x</sub> (red), Ru<sub>0.6</sub>Cr<sub>0.4</sub>O<sub>x</sub> (yellow), and RuO<sub>x</sub> (dark blue). (c) Mass activity at 1.48 V vs RHE (250 mV overpotential) normalized by the total mass of Ru in the catalyst for Ru<sub>0.6</sub>Cr<sub>0.2</sub>Ti<sub>0.2</sub>O<sub>x</sub> (red), Ru<sub>0.6</sub>Cr<sub>0.4</sub>O<sub>x</sub> (yellow), and RuO<sub>x</sub> (dark blue). (d) Stability test in a PEM water electrolyzer held at constant current density of 100 mA·cm<sup>-2</sup><sub>geo</sub> in the 0.05 M H<sub>2</sub>SO<sub>4</sub> electrolyte and using a Nafion 117 membrane. (e) Three-electrode chronopotentiometry (CP) test for Ru<sub>0.6</sub>Cr<sub>0.2</sub>Ti<sub>0.2</sub>O<sub>x</sub> at 10 mA·cm<sup>-2</sup><sub>geo</sub> in a 0.5 M H<sub>2</sub>SO<sub>4</sub> electrolyte. (f) Accumulative total dissolved ions for RuO<sub>x</sub> and Ru<sub>0.6</sub>Cr<sub>0.2</sub>Ti<sub>0.2</sub>O<sub>x</sub> in the 0.5 M H<sub>2</sub>SO<sub>4</sub> electrolyte. The electrolyte samples were collected post-OER at 10 mA·cm<sup>-2</sup><sub>geo</sub> over varying time periods.

The electrocatalysts were then deposited on carbon substrates to achieve a mass loading of 0.5 mg·cm<sup>-2</sup>. Linear sweep voltammetry at 5 mV·s<sup>-1</sup> was carried out in 0.5 M H<sub>2</sub>SO<sub>4</sub> to evaluate the OER activity of the catalysts (Figure 3a). We found that doping Ti in Ru<sub>0.75</sub>Cr<sub>0.25</sub>O<sub>x</sub> increased the overpotential slightly by ca. 12 mV (±2 mV) compared to Ru<sub>0.75</sub>Cr<sub>0.25</sub>O<sub>x</sub> but maintained a Tafel slope (58 mV dec<sup>-1</sup>) similar to Ru<sub>0.75</sub>Cr<sub>0.25</sub>O<sub>x</sub> (56 mV dec<sup>-1</sup>) and RuO<sub>x</sub> (54 mV dec<sup>-1</sup>) implying similar reaction kinetics (Figure 3b). When we

normalized the activity [at 1.48 V vs reverse hydrogen electrode (RHE)] by the total mass of Ru in the samples, we found that the mass activities of the Ru<sub>0.75</sub>Cr<sub>0.25</sub>O<sub>x</sub> (433 A g<sub>Ru</sub><sup>-1</sup>) and Ru<sub>0.6</sub>Cr<sub>0.2</sub>Ti<sub>0.2</sub>O<sub>x</sub> (475 A g<sub>Ru</sub><sup>-1</sup>) samples were similar and approximately 4 times higher than RuO<sub>x</sub> (79 A g<sub>Ru</sub><sup>-1</sup>) (Figure 3c). The comparable mass activities of Ru<sub>0.75</sub>Cr<sub>0.25</sub>O<sub>x</sub> and Ru<sub>0.6</sub>Cr<sub>0.2</sub>Ti<sub>0.2</sub>O<sub>x</sub> suggest that Ti did not contribute to enhancing the specific activity of the electrocatalyst. Instead, Cr appears to be the consistent element

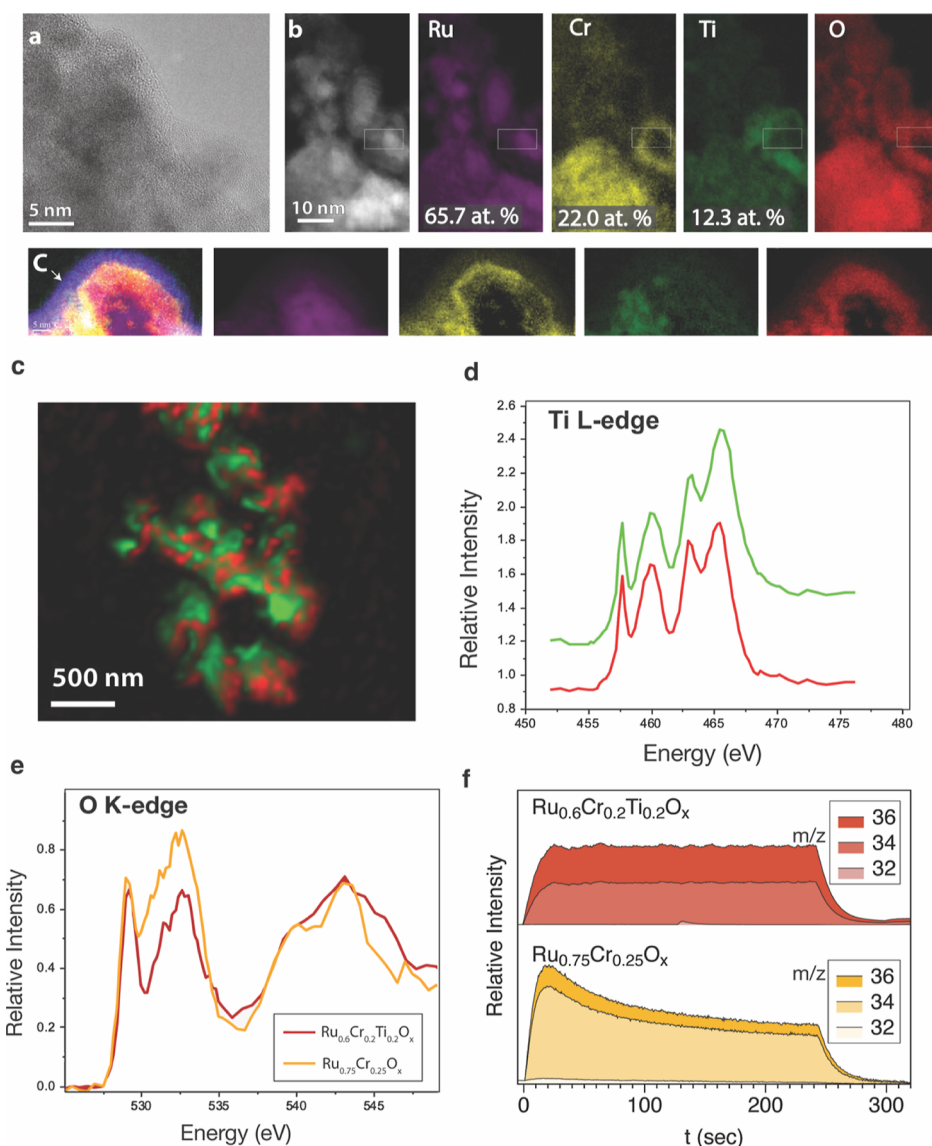


**Figure 4.** (a) High-resolution TEM image of the catalyst post-OER. (b) STEM image and elemental maps of the catalyst post-OER. STXM spectroptychography analysis of  $\text{Ru}_{0.6}\text{Cr}_{0.2}\text{Ti}_{0.2}\text{O}_x$ . (c) X-ray optical density map averaged from 452 to 476 eV, red and green for thin and thick regions, respectively. (d) Ti L-edge X-ray absorption spectrum for the regions highlighted in the optical density map. (e) O K-edge STXM spectroptychography XANES comparison between  $\text{Ru}_{0.75}\text{Cr}_{0.25}\text{O}_x$  and  $\text{Ru}_{0.6}\text{Cr}_{0.2}\text{Ti}_{0.2}\text{O}_x$ . (f) DEMS signals of  $^{36}\text{O}_2$  ( $^{18}\text{O}^{18}\text{O}$ ),  $^{34}\text{O}_2$  ( $^{16}\text{O}^{18}\text{O}$ ), and  $^{32}\text{O}_2$  ( $^{16}\text{O}^{16}\text{O}$ ) from the reaction products using a  $\text{H}_2$   $^{18}\text{O}$  aqueous sulfuric acid electrolyte. The mass spectroscopy signals are the baseline subtracted.

associated with the improvement in mass activity. Electrochemical surface area (ECSA) measurements of the catalysts (Figures S14 and S15) revealed that adding Cr significantly increased the surface area of the catalyst by a factor of ca. 7 compared to  $\text{RuO}_x$  implying that improvements in the geometric activity can arise from an increase in the surface area when doping Cr. However, despite the increase in the surface area, the ECSA-normalized activity of  $\text{Ru}_{0.6}\text{Cr}_{0.2}\text{Ti}_{0.2}\text{O}_x$  was still the highest, suggesting a synergistic effect in the metal mix improving the intrinsic activity of the electrocatalyst (Figure S16). The role of Cr in activity will be further elucidated using DFT later in this work.

**Electrochemical Stability.** We then investigated the stability of the samples by CP at  $10 \text{ mA}\cdot\text{cm}^{-2}$  (Figure S17). We did not see any significant changes in the overpotential of the samples in the first 10 h. Therefore, we decided to test the catalysts at a higher current density ( $100 \text{ mA}\cdot\text{cm}^{-2}$ ) in a PEM

water electrolyzer fed with room-temperature  $0.05 \text{ M H}_2\text{SO}_4$  (Figure 3d) to test the electrocatalysts under accelerated degradation conditions. Within the first 40 h, both  $\text{RuO}_x$  and  $\text{Ru}_{0.75}\text{Cr}_{0.25}\text{O}_x$  have incurred massive overpotentials leading to entire deactivation at the end of the test. However, the Ti-doped sample demonstrated stable water electrolysis for 200 h with a minor increase in full cell voltage (5 mV) throughout the test, a much lower increase rate than other electrocatalysts reported in the literature (Table S9).

To elucidate the origin of the stability of the  $\text{Ru}_{0.6}\text{Cr}_{0.2}\text{Ti}_{0.2}\text{O}_x$  catalyst, we run a long CP test at  $10 \text{ mA}\cdot\text{cm}^{-2}$  for 1100 h (Figure 3e). We noticed a drastic increase in overpotential (36 mV) over the first 100 h of testing, followed by less than 8 mV over the rest of the test ( $8 \mu\text{V h}^{-1}$ ). We switched off the current supply and then turned it on at the 500 h mark and we observed that the performance was retained immediately with no noticeable changes in the



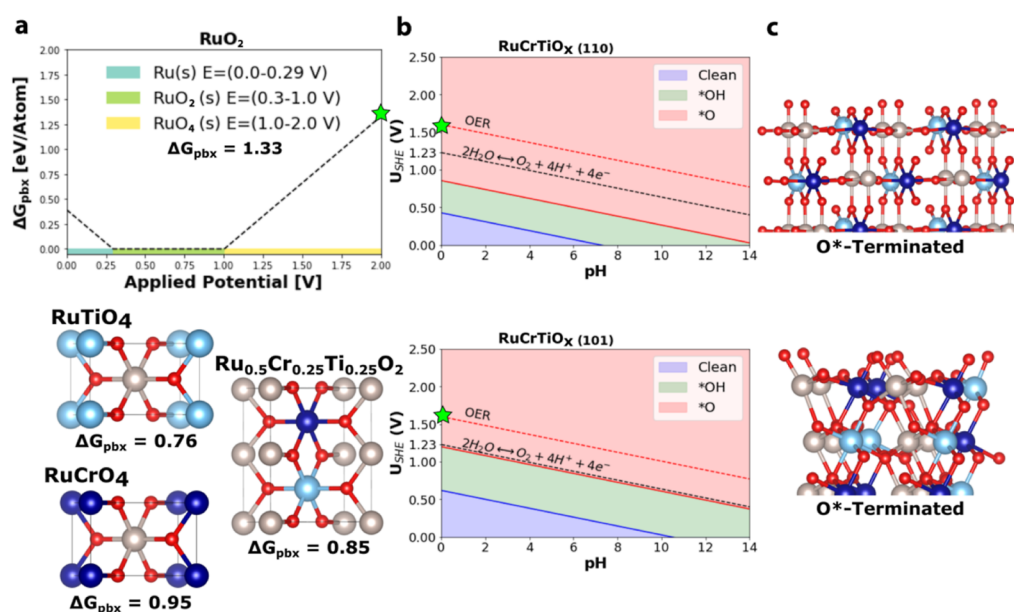


**Figure 5.** (a) Calculated Pourbaix decomposition free energy  $\Delta G_{\text{pbx}}$  of  $\text{RuO}_2$ ,  $\text{RuTiO}_4$ ,  $\text{RuCrO}_4$ , and  $\text{Ru}_{0.5}\text{Cr}_{0.25}\text{Ti}_{0.25}\text{O}_2$  from the potential 0–2.0 V (vs SHE) at pH = 0. (b)  $\text{RuCrTiO}_x$  surface Pourbaix diagrams for the (110) and (101) with three different regions: clean (blue),  $\text{OH}^*$  (green), and  $\text{O}^*$  (red) as full saturated terminations. (c)  $\text{RuCrTiO}_x$  slab models for the (110) and (101) with  $\text{O}^*$  as the most stable termination at ( $U = 1.60 \text{ V}$ , pH = 0). \*The green star indicates the selected value both in bulk stability and surface Pourbaix diagram.

overpotential. During the test, we monitored the dissolution of metal ions using ICP-AES. We observed a dramatic increase in the Ru dissolution rate for  $\text{RuO}_x$  within 48 h (Figures 3f and S18, Table S8). On the other hand, the dissolution rate of Ru in the  $\text{Ru}_{0.6}\text{Cr}_{0.2}\text{Ti}_{0.2}\text{O}_x$  sample was held to <1 wt % loss throughout the stability test with a ca. 20 times slower dissolution rate than  $\text{RuO}_x$  (Figure S18). The Cr dissolution was kept <0.1 wt % and the dissolution rate of Ti was increasing at 0.005 wt % loss every hour. The change in dissolution rates within the first 48 h suggests that the electrocatalyst has undergone an activation period changing its initial structure.

Consequently, we looked at the morphology and chemical changes of the electrocatalyst after the OER to explain the improved stability (Figure 4a,b). The TEM images showed a finite amorphous layer covering the nanocrystals which is mainly composed of carbon from contamination as indicated by the electron energy loss spectrometer maps. The elemental maps clearly showed a thin layer rich in Cr over the Ru core by forming a porous, hydrous Cr–O surface layer during activation. The presence of the hydrous Cr–O layer was also supported by observing a small increase in the Cr–O bond in EXAFS of Cr K-edge (Figure S19). Because we did not observe any additional stability improvements from incorporating Cr into  $\text{RuO}_2$  ( $\text{Ru}_{0.75}\text{Cr}_{0.25}\text{O}_x$ ), as shown in Figure 3d, we believe that the formation of the Cr–O surface layer does not contribute significantly to improving stability. Looking at the EDS elemental map of Ti, we hypothesize that Ti formed strong oxo-bonds while slowly dissolving in acid, which infers that much of Ti may have formed a strong Ti–O network with surface Ru and Cr. The presence of strong Ti oxo bonds during OER was confirmed using in situ XAS (Figure S20) as inferred by the right shift of the XANES K-edge of Ti (higher binding energy) and the left shift of the Ti–O in EXAFS (shorter bond) at 1.4 V vs RHE. The XAS spectra of Ru remained unchanged during OER indicating that Ru atoms were stabilized in the rutile oxide lattice (Figure S21).

To study experimentally the role of increased metal–oxygen covalency on stabilizing Ru, we used STXM spectroscopy to chemically map (with a high spatial resolution ca. 10 nm) and compare the X-ray spectral differences between  $\text{Ru}_{0.6}\text{Cr}_{0.2}\text{Ti}_{0.2}\text{O}_x$  and  $\text{Ru}_{0.75}\text{Cr}_{0.25}\text{O}_x$  nanoparticles. Two representative uniform regions in the samples were detected: a thick bright region labeled 1 and a thin region labeled 2 (Figures S22a and S23a). The thick region (1) in both samples reflects undesired oxidation and agglomeration of particles during sample preparation. The difference in the nature of the oxide in the two regions could be clearly differentiated by comparing the two O K-edge XANES profiles at 537–550 eV (Figures S22b and S23b) and comparing the energy shifts at the Cr L-edge (Figures S22c and S23c). The negative shift in the spectrum taken from region 2 compared to region 1 indicated a less degree of oxidation, closer to expectations. Therefore, we only considered region 2 for our analysis.

The features appearing in the Ti L-edge across the sample are characteristic of rutile Ti,<sup>19</sup> confirming the incorporation of Ti in the rutile lattice as previously shown by Ti K-edge XAS and XRD (Figure 4c,d). The rutile lattice of the samples was further confirmed by looking at the spectral features of Cr L-edge (Figures S22c and S23c) and Ru M-edge (Figure S24) and comparing them to  $\text{RuO}_2$  and  $\text{CrO}_2$  from the literature.<sup>20,21</sup> We found that the oxidation state of Ru and Cr in both of our samples is 4+. Moreover, an obvious increase in an intensity ratio of 530 eV peak over 543 eV peak in O K-edge, as seen in Figure 4e, suggested a significant increase of the metal–oxygen covalency in  $\text{Ru}_{0.6}\text{Cr}_{0.2}\text{Ti}_{0.2}\text{O}_x$  relative to that in  $\text{Ru}_{0.75}\text{Cr}_{0.25}\text{O}_x$ .<sup>19</sup> This increase in covalency was predicted earlier in this work by the COHP computational pipeline for Ru–Ti– $\text{O}_x$ . Using the same computational method, we calculated the metal–oxygen covalency of Ru–Cr–Ti– $\text{O}_x$  and found that it was 93.62%, which remained considerably higher than  $\text{RuO}_2$  (85.20%) and slightly less (2.3% lower) than Ru–Ti– $\text{O}_x$  due to the addition of Cr.

**Table 1.** Calculated Surface Energies, Binding Free Energies of O\*, OH\*, and OOH\*, Theoretical Overpotential  $\eta_{\text{OER}}$ , and PDS for all the Considered Surfaces and Materials<sup>a</sup>

(hkl)	formula	$\gamma_{\text{hkl}}$ (J/m <sup>2</sup> )	$\Delta G_{\text{OH}^*}$ (eV)	$\Delta G_{\text{O}^*}$ (eV)	$\Delta G_{\text{GOOH}^*}$ (eV)	$\Delta G_{\text{O}^*} - \Delta G_{\text{OH}^*}$ (eV)	$\Delta G_{\text{GOOH}^*} - \Delta G_{\text{O}^*}$ (eV)	$\eta_{\text{OER}}$ (V)	PDS
(110)	RuO <sub>2</sub>	0.96	0.48	1.88	3.63	1.41	1.75	0.52	O* → OOH*
	RuTiO <sub>4</sub>	0.74	0.15	1.33	3.22	1.19	1.89	0.66	O* → OOH*
	RuCrO <sub>4</sub>	0.86	0.66	1.95	3.76	1.30	1.81	0.58	O* → OOH*
	RuCrTiO <sub>x</sub>	0.87	0.55	1.74	3.35	1.19	1.62	0.39	O* → OOH*
(101)	RuO <sub>2</sub>	1.05	0.43	2.19	3.67	1.76	1.48	0.53	OH* → O*
	RuTiO <sub>4</sub>	0.95	0.26	1.47	3.21	1.22	1.73	0.50	O* → OOH*
	RuCrO <sub>4</sub>	1.09	0.69	2.11	3.58	1.42	1.47	0.24	O* → OOH*
	RuCrTiO <sub>x</sub>	1.34	0.39	2.09	3.83	1.71	1.71	0.50	O* → OOH*

<sup>a</sup>All the explored OER intermediates are in Section S7.

We further conducted in situ DEMS measurements using the <sup>18</sup>O isotope to investigate the participation of lattice oxygen in the reaction. We used H<sub>2</sub><sup>18</sup>O aqueous H<sub>2</sub>SO<sub>4</sub> electrolytes and measured the evolved O<sub>2</sub> during OER by running a chronoamperometry at 1.8 V (vs RHE) for 5 min (Figure 4f, see S3 Experimental methods in the Supporting Information). The amount of <sup>34</sup>O<sub>2</sub> evolved reflected the participation of lattice oxygen coming from the combination of <sup>16</sup>O in the lattice and <sup>18</sup>O in the electrolyte. The ratio of <sup>34</sup>O<sub>2</sub>/<sup>36</sup>O<sub>2</sub> generated on Ru<sub>0.6</sub>Cr<sub>0.2</sub>Ti<sub>0.2</sub>O<sub>x</sub> was much lower than that on Ru<sub>0.75</sub>Cr<sub>0.25</sub>O<sub>x</sub>. As a result, incorporating Ti in the lattice suppressed lattice oxygen participation by ~66% on Ru<sub>0.6</sub>Cr<sub>0.2</sub>Ti<sub>0.2</sub>O<sub>x</sub> compared to that on Ru<sub>0.75</sub>Cr<sub>0.25</sub>O<sub>x</sub>. Our findings indicate that the excessive dissolution of Ru in Ru<sub>0.75</sub>Cr<sub>0.25</sub>O<sub>x</sub> is associated with a larger lattice oxidation evolution compared to Ru<sub>0.6</sub>Cr<sub>0.2</sub>Ti<sub>0.2</sub>O<sub>x</sub>. This aligns with the observation made by Scott et al., suggesting that a significant increase in lattice oxidation evolution is triggered by an increase in dissolution.<sup>22</sup> We propose that the enhanced metal–oxygen covalency in Ru<sub>0.6</sub>Cr<sub>0.2</sub>Ti<sub>0.2</sub>O<sub>x</sub> results in a more rigid metal–oxygen framework and increases the kinetic barriers for oxide dissolution. This ultimately leads to a more stable electrocatalyst. This relationship between metal–oxygen covalency and stability of electrocatalysts was also observed by Shao-Horn and co-workers in perovskites and manganese oxides for OER.<sup>23,24</sup>

**Computational Surface Diagrams and OER Reactivity.** To accurately calculate the theoretical OER activity from DFT and validate experimental results, it is important to find the most stable surface termination under real reaction conditions. Surface selection could impact the local environment of the active site, resulting in significant changes in calculating the adsorption interaction of the OER intermediates with the electrocatalyst. In Figure 5b, we show the surface Pourbaix diagrams for both Ru–Cr–TiO<sub>x</sub> (110) and (101) facets with 3 well-defined regions: (i) clean, (ii) OH\*, and (iii) O\* terminations. All of the computed intermediates can be found in the Supporting Information Section S6. The most stable termination among all of the compositions in this work was found to be the O\* terminated (Figure 5c). We then selected the corresponding structure to the most stable coverage at 1.60 V vs RHE for further activity calculations.

The OER activity data for RuO<sub>2</sub>, RuTiO<sub>4</sub>, RuCrO<sub>4</sub>, and RuCrTiO<sub>x</sub> considering both (110) and (101) surfaces with O\*-termination (as determined by the surface Pourbaix diagrams) is summarized in Table 1. The OER mechanism was modeled as the water nucleophilic attack on top of a single Ru active site for all surfaces (see Supporting Information,

Section S7 and computational details in Section S2). All the DFT modeling was carried out in an automated fashion, available openly, using the WhereWulff package (<https://github.com/ulissigroup/wherewulff>).<sup>25</sup>

The Ru atoms were selected as the active site for both the (110) and (101) surfaces, which exhibit an octahedral (Oh) coordination environment across all compositions. In this regard, (110) surfaces expose the axial position as an available coordination site to perform the OER mechanism, whereas (101) surfaces are equatorial coordination sites. This coordination difference impacts the general  $\Delta G$  of adsorption, being stronger at the axial position, usually translated as slightly higher overpotentials, compared to those at equatorial positions, which are usually weaker interactions corresponding to lower overpotentials, as already seen in the literature.<sup>26,27</sup> Furthermore, the potential determining step (PDS) is generally located at the third proton-coupled electron transfer step, which is the nucleophilic attack of water coming from the solvent to the activated O\* species on both the (110) and (101), although on the pure RuO<sub>2</sub> (101) facet the PDS is the formation of the O\* from the OH\* species.

On the one hand, incorporating Ti in the RuO<sub>2</sub> rutile structure enhanced the overall electrochemical stability, as shown in the previous sections, but the calculated catalytic activity was slightly lowered compared to RuO<sub>2</sub> (Table 1). On the other hand, substituting Cr in the lattice was found not to play a significant role in improving the electrochemical stability, yet it resulted in higher catalytic activity compared to RuO<sub>2</sub>. This improvement can be seen for the (101) surface, which is the most contributing surface to the nanoparticle structure due to its 8 equiv Miller indices coming from the rutile structure symmetry. When both Cr and Ti are incorporated in the lattice, such in RuCrTiO<sub>x</sub>, the overpotential values of 0.39/0.50 V for the (110) and (101) surfaces, respectively, still show activity improvements compared to that of RuO<sub>2</sub>. These results match very well with our experimental observation and unearth the respective roles of Ti and Cr in the activity of the electrocatalyst.

The improved performance shown for RuCrO<sub>4</sub> (101) originated from a synergistic relationship between Ru and the nearest Cr atom, forming a Ru–O–Cr dimer. The  $\Delta G(\text{OH}^*)$  at the RuCrO<sub>4</sub> (101) intermediate was strongly affected because of the weaker intra OH\*...O\* hydrogen bond compared to RuO<sub>2</sub> and RuTiO<sub>4</sub>. This led to less stable OH\* species on the surface. This intrahydrogen bond distance between the OH\* and O\* specie varied from 1.707 Å (RuO<sub>2</sub>) to 1.925 Å (RuCrTiO<sub>x</sub>), where the longest distance (the weaker interaction) was observed for RuCrO<sub>4</sub> with 2.011 Å.



Furthermore, we characterized the intrahydrogen bond OH\*...O\* interaction through the charge density difference and the Bader charges of OH\* species for the RuO<sub>2</sub>, RuTiO<sub>4</sub>, RuCrO<sub>4</sub>, and RuCrTiO<sub>x</sub> compositions on top of the (101) facet (Figure S35). Interestingly, the Bader charges along the Ru–OH\* part of the dimer stay similar across compositions, but the Cr=O\* and specifically the charge located at the O\* atom correlates with the  $\Delta G(\text{OH}^*)$  as RuTiO<sub>4</sub> < RuCrTiO<sub>x</sub> < RuO<sub>2</sub>  $\ll$  RuCrO<sub>4</sub> showing that the Cr=O\* part of the dimer forces an acidic O\* species compared to the other intermediates and therefore weakening the intra hydrogen bond and destabilizing the Ru–OH\* intermediate. Moreover, we computed the d-band center of the Ru d orbital for each candidate to gain insights into electronic effects. We noted a general trend where the d-band center shift from the Fermi level for RuCrO<sub>4</sub> (−1.12 eV) is larger than that for RuO<sub>2</sub> (−0.7 eV), consistent with the destabilization of the \*O adsorption energy (Figure S36).

## CONCLUSIONS

In this work, we developed a ML-aided computational pipeline that screened the Pourbaix energy for 2070 oxides to assess their electrochemical stability under acidic OER. We used metal–oxygen covalency as a secondary screening descriptor to predict the bulk stability of the oxide. By combining this computational descriptor screening approach with experiments, we found that substituting Cr and Ti in the RuO<sub>2</sub> lattice drastically improved the activity and stability compared to pure RuO<sub>2</sub>. Through experimentally optimizing the Cr content in RuO<sub>2</sub>, we lowered the overpotential by 70 mV compared to that in pure RuO<sub>2</sub>. Then, we computationally studied the influence of doping Cr on activity and discovered that the formed Ru–O–Cr dimer had a synergistic effect weakening the Ru–OH\* intermediate and, consequently, lowering the energy barrier of the PDS. Furthermore, a 20 at. % Ti was successfully incorporated in the Cr-doped RuO<sub>2</sub> lattice using a modified sol–gel synthesis and confirmed using XRD, XAS, and STXM. We found that Ti significantly extended the stability of RuO<sub>2</sub> from less than 20 h to at least 200 h at 100 mA·cm<sup>−2</sup>. Doping Ti in the lattice was found to result in a strong metal–oxygen covalency, as evident by the chemical shifts in STXM and XAS and as predicted by ML. Using TEM and in situ XAS, we confirmed that a metastable structure, composed of a Ti-oxo network and a Cr overlayer, formed during the reaction suppressing the dissolution of Ru by 20× as measured by ICP-AES. The design principles introduced in our computational pipeline could offer crucial insights into the development of stable metal oxides for electrochemical applications in acidic media.

## ASSOCIATED CONTENT

### Supporting Information

The Supporting Information is available free of charge at <https://pubs.acs.org/doi/10.1021/jacs.4c01353>.

CGCNN-HD model performance, DFT method, ML-HTS experimental methods, materials, synthesis, XRD, electron microscopy, ICP-AES, electrochemical testing, XAS, STXM, in situ DEMS, experimental figures, experimental tables, electrochemical performance, ICP measurements, and EXAFS fittings, computational surface diagrams, OER intermediates DFT figures,

charge density difference and Bader charges analysis, and projected density of states (PDF)

## AUTHOR INFORMATION

### Corresponding Authors

Zachary W. Ulissi – Department of Chemical Engineering, Carnegie Mellon University, Pittsburgh, Pennsylvania 15213, United States; Email: [zulissi@andrew.cmu.edu](mailto:zulissi@andrew.cmu.edu)

Edward H. Sargent – Department of Electrical and Computer Engineering, University of Toronto, Toronto, Ontario M5S 1A4, Canada; [orcid.org/0000-0003-0396-6495](https://orcid.org/0000-0003-0396-6495); Email: [ted.sargent@utoronto.ca](mailto:ted.sargent@utoronto.ca)

### Authors

Jehad Abed – Department of Materials Science and Engineering, University of Toronto, Toronto, Ontario M5S 3E4, Canada; Department of Electrical and Computer Engineering, University of Toronto, Toronto, Ontario M5S 1A4, Canada; [orcid.org/0000-0003-1387-2740](https://orcid.org/0000-0003-1387-2740)

Javier Heras-Domingo – Department of Chemical Engineering, Carnegie Mellon University, Pittsburgh, Pennsylvania 15213, United States; [orcid.org/0000-0002-4322-3146](https://orcid.org/0000-0002-4322-3146)

Rohan Yuri Sanspeur – Department of Chemical Engineering, Carnegie Mellon University, Pittsburgh, Pennsylvania 15213, United States; [orcid.org/0000-0002-5583-8922](https://orcid.org/0000-0002-5583-8922)

Mingchuan Luo – School of Materials Science and Engineering, Peking University, Beijing 100871, P. R. China

Wajdi Alnough – Department of Chemical Engineering, McMaster University, Hamilton, Ontario L8S 4L7, Canada

Debora Motta Meira – CLS@APS Sector 20, Advanced Photon Source, Argonne National Laboratory, Argonne, Illinois 60439, United States; Canadian Light Source Inc., Saskatoon, Saskatchewan S7N 2 V3, Canada

Hsiaotsu Wang – Canadian Light Source Inc., Saskatoon, Saskatchewan S7N 2 V3, Canada; [orcid.org/0000-0003-1249-9462](https://orcid.org/0000-0003-1249-9462)

Jian Wang – Canadian Light Source Inc., Saskatoon, Saskatchewan S7N 2 V3, Canada

Jigang Zhou – Canadian Light Source Inc., Saskatoon, Saskatchewan S7N 2 V3, Canada; [orcid.org/0000-0001-6644-2862](https://orcid.org/0000-0001-6644-2862)

Daojin Zhou – Department of Electrical and Computer Engineering, University of Toronto, Toronto, Ontario M5S 1A4, Canada

Khalid Fatih – Clean Energy Innovation, National Research Council Canada, Vancouver, British Columbia V6T 1W5, Canada

John R. Kitchin – Department of Chemical Engineering, Carnegie Mellon University, Pittsburgh, Pennsylvania 15213, United States; [orcid.org/0000-0003-2625-9232](https://orcid.org/0000-0003-2625-9232)

Drew Higgins – Department of Chemical Engineering, McMaster University, Hamilton, Ontario L8S 4L7, Canada; [orcid.org/0000-0002-0585-2670](https://orcid.org/0000-0002-0585-2670)

Complete contact information is available at: <https://pubs.acs.org/doi/10.1021/jacs.4c01353>

### Author Contributions

○J.A., J.H.D., and R.Y.S. contributed equally to this paper.

### Notes

The authors declare no competing financial interest.

## ACKNOWLEDGMENTS

This work was supported financially by the National Research Council (NRC) of Canada, the Natural Sciences and Engineering Research Council (NSERC) of Canada, a Vanier Canada Graduate Scholarship, and the Army Research Office (ARO) project Award W911NF2010188. Electron microscopy, scanning transmission electron microscopy, and electron energy loss spectroscopy were performed at the Canadian Centre for Electron Microscopy (CCEM) at McMaster University. STXM ptychography was performed at the SM beamline at the Canadian Light Source, a national research facility of the University of Saskatchewan, which is supported by the Canada Foundation for Innovation (CFI), NSERC, NRC, the Canadian Institutes of Health Research (CIHR), the Government of Saskatchewan, and the University of Saskatchewan. This research used resources of the Advanced Photon Source, an Office of Science User Facility operated for the U.S. Department of Energy (DOE) Office of Science by Argonne National Laboratory and was supported by the U.S. DOE under contract no. DE-AC02-06CH11357, and the Canadian Light Source and its funding partners. The authors thank Dr. Tianpin Wu and Dr. George Sterbinsky from 9BM beamline, and Debora Motta Meira and Zou Finckro from 20BM beamline for assistance in collecting the XAS data and at the advanced photo source (APS). This paper is an adaptation of the author's thesis titled "Developing Efficient Electrocatalysts for Oxygen Evolution at High Current Densities" submitted to University of Toronto.

## REFERENCES

- (1) Danilovic, N.; Subbaraman, R.; Chang, K.-C.; Chang, S. H.; Kang, Y. J.; Snyder, J.; Paulikas, A. P.; Strmcnik, D.; Kim, Y.-T.; Myers, D.; Stamenkovic, V. R.; Markovic, N. M. Activity-Stability Trends for the Oxygen Evolution Reaction on Monometallic Oxides in Acidic Environments. *J. Phys. Chem. Lett.* **2014**, *5* (14), 2474–2478.
- (2) Blasco-Ahicart, M.; Soriano-Lopez, J.; Carbo, J. J.; Poblet, J. M.; Galan-Mascaros, J. R. Polyoxometalate Electrocatalysts Based on Earth-Abundant Metals for Efficient Water Oxidation in Acidic Media. *Nat. Chem.* **2017**, *10* (1), 24–30.
- (3) Shan, J.; Guo, C.; Zhu, Y.; Chen, S.; Song, L.; Jaroniec, M.; Zheng, Y.; Qiao, S. Z. Charge-Redistribution-Enhanced Nanocrystalline Ru@IrOx Electrocatalysts for Oxygen Evolution in Acidic Media. *Chem* **2019**, *5* (2), 445–459.
- (4) Hao, S.; Liu, M.; Pan, J.; Liu, X.; Tan, X.; Xu, N.; He, Y.; Lei, L.; Zhang, X. Dopants Fixation of Ruthenium for Boosting Acidic Oxygen Evolution Stability and Activity. *Nat. Commun.* **2020**, *11* (1), 5368.
- (5) Lin, Y.; Tian, Z.; Zhang, L.; Ma, J.; Jiang, Z.; Deibert, B. J.; Ge, R.; Chen, L. Chromium-Ruthenium Oxide Solid Solution Electrocatalyst for Highly Efficient Oxygen Evolution Reaction in Acidic Media. *Nat. Commun.* **2019**, *10* (1), 162.
- (6) Yao, Y.; Hu, S.; Chen, W.; Huang, Z.-Q.; Wei, W.; Yao, T.; Liu, R.; Zang, K.; Wang, X.; Wu, G.; Yuan, W.; Yuan, T.; Zhu, B.; Liu, W.; Li, Z.; He, D.; Xue, Z.; Wang, Y.; Zheng, X.; Dong, J.; Chang, C.-R.; Chen, Y.; Hong, X.; Luo, J.; Wei, S.; Li, W.-X.; Strasser, P.; Wu, Y.; Li, Y. Engineering the Electronic Structure of Single Atom Ru Sites via Compressive Strain Boosts Acidic Water Oxidation Electrocatalysis. *Nat. Catal.* **2019**, *2* (4), 304–313.
- (7) Gu, G. H.; Noh, J.; Kim, S.; Back, S.; Ulissi, Z.; Jung, Y. Practical Deep-Learning Representation for Fast Heterogeneous Catalyst Screening. *J. Phys. Chem. Lett.* **2020**, *11* (9), 3185–3191.
- (8) Flores, R. A.; Paolucci, C.; Winther, K. T.; Jain, A.; Torres, J. A. G.; Aykol, M.; Montoya, J.; Nørskov, J. K.; Bajdich, M.; Bligaard, T. Active Learning Accelerated Discovery of Stable Iridium Oxide Polymorphs for the Oxygen Evolution Reaction. *Chem. Mater.* **2020**, *32* (13), 5854–5863.
- (9) Choudhary, K.; DeCost, B.; Tavazza, F. Machine Learning with Force-Field-Inspired Descriptors for Materials: Fast Screening and Mapping Energy Landscape. *Phys. Rev. Mater.* **2018**, *2* (8), 083801.
- (10) Noh, J.; Gu, G. H.; Kim, S.; Jung, Y. Uncertainty-Quantified Hybrid Machine Learning/Density Functional Theory High Throughput Screening Method for Crystals. *J. Chem. Inf. Model.* **2020**, *60* (4), 1996–2003.
- (11) Jain, A.; Ong, S. P.; Hautier, G.; Chen, W.; Richards, W. D.; Dacek, S.; Cholia, S.; Gunter, D.; Skinner, D.; Ceder, G.; Persson, K. A. Commentary: The Materials Project: A Materials Genome Approach to Accelerating Materials Innovation. *APL Mater.* **2013**, *1* (1), 011002.
- (12) Sendek, A. D.; Yang, Q.; Cubuk, E. D.; Duerloo, K. A. N.; Cui, Y.; Reed, E. J. Holistic Computational Structure Screening of More than 12000 Candidates for Solid Lithium-Ion Conductor Materials. *Energy Environ. Sci.* **2017**, *10* (1), 306–320.
- (13) Maintz, S.; Deringer, V. L.; Tchougréeff, A. L.; Dronskowski, R. LOBSTER: A Tool to Extract Chemical Bonding from Plane-Wave Based DFT. *J. Comput. Chem.* **2016**, *37* (11), 1030–1035.
- (14) Sun, W.; Bartel, C. J.; Arca, E.; Bauers, S. R.; Matthews, B.; Orvañanos, B.; Chen, B.-R.; Toney, M. F.; Schelhas, L. T.; Tumas, W.; Tate, J.; Zakutayev, A.; Lany, S.; Holder, A. M.; Ceder, G. A Map of the Inorganic Ternary Metal Nitrides. *Nat. Mater.* **2019**, *18* (7), 732–739.
- (15) Wang, Z.; Zheng, Y.-R.; Chorkendorff, I.; Nørskov, J. K. Acid-Stable Oxides for Oxygen Electrocatalysis. *ACS Energy Lett.* **2020**, *5* (9), 2905–2908.
- (16) Gunasooriya, G. T. K. K.; Nørskov, J. K. Analysis of Acid-Stable and Active Oxides for the Oxygen Evolution Reaction. *ACS Energy Lett.* **2020**, *5* (12), 3778–3787.
- (17) Choubisa, H.; Abed, J.; Mendoza, D.; Matsumura, H.; Sugimura, M.; Yao, Z.; Wang, Z.; Sutherland, B. R.; Aspuru-Guzik, A.; Sargent, E. H. Accelerated Chemical Space Search Using a Quantum-Inspired Cluster Expansion Approach. *Matter* **2023**, *6* (2), 605–625.
- (18) Chu, I.-H.; Roychowdhury, S.; Han, D.; Jain, A.; Ong, S. P. Predicting the Volumes of Crystals. *Comput. Mater. Sci.* **2018**, *146*, 184–192.
- (19) Zhou, J. G.; Fang, H. T.; Maley, J. M.; Murphy, M. W.; Peter Ko, J. Y.; Cutler, J. N.; Sammynaiken, R.; Sham, T. K.; Liu, M.; Li, F. Electronic Structure of TiO<sub>2</sub> nanotube Arrays from X-Ray Absorption near Edge Structure Studies. *J. Mater. Chem.* **2009**, *19* (37), 6804–6809.
- (20) Zhou, J.; Wang, J.; Fang, H.; Wu, C.; Cutler, J. N.; Sham, T. K. Nanoscale Chemical Imaging and Spectroscopy of Individual RuO<sub>2</sub> Coated Carbon Nanotubes. *Chem. Commun.* **2010**, *46* (16), 2778–2780.
- (21) Frati, F.; Hunault, M. O. J. Y.; De Groot, F. M. F. Oxygen K-Edge X-Ray Absorption Spectra. *Chem. Rev.* **2020**, *120* (9), 4056–4110.
- (22) Scott, S. B.; Sørensen, J. E.; Rao, R. R.; Moon, C.; Kibsgaard, J.; Shao-Horn, Y.; Chorkendorff, I. The Low Overpotential Regime of Acidic Water Oxidation Part II: Trends in Metal and Oxygen Stability Numbers. *Energy Environ. Sci.* **2022**, *15* (5), 1988–2001.
- (23) Stoerzinger, K. A.; Hong, W. T.; Wang, X. R.; Rao, R. R.; Bengaluru Subramanyam, S.; Li, C.; Ariando; Venkatesan, T.; Liu, Q.; Crumlin, E. J.; Varanasi, K. K.; Shao-Horn, Y. Decreasing the Hydroxylation Affinity of La<sub>1-x</sub>Sr<sub>x</sub>MnO<sub>3</sub> Perovskites To Promote Oxygen Reduction Electrocatalysis. *Chem. Mater.* **2017**, *29* (23), 9990–9997.
- (24) Peng, J.; Giordano, L.; Davenport, T. C.; Shao-Horn, Y. Stability Design Principles of Manganese-Based Oxides in Acid. *Chem. Mater.* **2022**, *34* (17), 7774–7787.
- (25) Sanspeur, R. Y.; Heras-Domingo, J.; Kitchin, J. R.; Ulissi, Z. WhereWulff: A Semiautonomous Workflow for Systematic Catalyst Surface Reactivity under Reaction Conditions. *J. Chem. Inf. Model.* **2023**, *63* (8), 2427–2437.

(26) Ping, Y.; Nielsen, R. J.; Goddard, W. A. The Reaction Mechanism with Free Energy Barriers at Constant Potentials for the Oxygen Evolution Reaction at the IrO<sub>2</sub> (110) Surface. *J. Am. Chem. Soc.* **2017**, *139* (1), 149–155.

(27) González, D.; Heras-Domingo, J.; Sodupe, M.; Rodríguez-Santiago, L.; Solans-Monfort, X. Importance of the Oxyl Character on the IrO<sub>2</sub> Surface Dependent Catalytic Activity for the Oxygen Evolution Reaction. *J. Catal.* **2021**, *396*, 192–201.